Science Translational Medicine

Wireless sensors for continuous, multimodal measurements at the skin interface with lower limb prostheses

Jean Won Kwak, Mengdi Han, Zhaoqian Xie, Ha Uk Chung, Jong Yoon Lee, Raudel Avila, Jessica Yohay, Xuexian Chen, Cunman Liang, Manish Patel, Inhwa Jung, Jongwon Kim, Myeong Namkoong, Kyeongha Kwon, Xu Guo, Christopher Ogle, Dominic Grande, Dennis Ryu, Dong Hyun Kim, Surabhi Madhvapathy, Claire Liu, Da Som Yang, Yoonseok Park, Ryan Caldwell, Anthony Banks, Shuai Xu, Yonggang Huang, Stefania Fatone and John A. Rogers

Sci Transl Med **12**, eabc4327.
DOI: 10.1126/scitranslmed.abc4327

Form, fit, and function

Improper fit between the prosthetic socket and the residual limb of persons with amputation causes discomfort, pressure ulcers, and altered load bearing. Kwak and colleagues developed pressure and temperature sensors to monitor the interface between a prosthesis and residual limb. The soft sensors communicated wirelessly with portable electronic devices during walking, sitting, and standing in non-amputees wearing prosthesis simulators and in two individuals with transtibial and transfemoral amputation, respectively. Results support use of wireless sensors to monitor the skin-prosthesis interface.

Science Translational Medicine (ISSN 1946-6242) is published by the American Association for the Advancement of Science, 1200 New York Avenue NW, Washington, DC 20005. The title *Science Translational Medicine* is a registered trademark of AAAS.

Science Translational Medicine
AAAS

stm.sciencemag.org/cgi/content/full/12/574/eabc4327/DC1

Supplementary Materials for

Wireless sensors for continuous, multimodal measurements at the skin interface with lower limb prostheses

Jean Won Kwak, Mengdi Han, Zhaoqian Xie, Ha Uk Chung, Jong Yoon Lee, Raudel Avila, Jessica Yohay, Xuexian Chen, Cunman Liang, Manish Patel, Inhwa Jung, Jongwon Kim, Myeong Namkoong, Kyeongha Kwon, Xu Guo, Christopher Ogle, Dominic Grande, Dennis Ryu, Dong Hyun Kim, Surabhi Madhvapathy, Claire Liu, Da Som Yang, Yoonseok Park, Ryan Caldwell, Anthony Banks, Shuai Xu, Yonggang Huang, Stefania Fatone, John A. Rogers*

*Corresponding author. Email: jrogers@northwestern.edu

Published 16 December 2020, *Sci. Transl. Med.* **12**, eabc4327 (2020)
DOI: 10.1126/scitranslmed.abc4327

The PDF file includes:

Other Supplementary Material for this manuscript includes the following:

(available at stm.sciencemag.org/cgi/content/full/12/574/eabc4327/DC1)

Data file S1 (Microsoft Excel format). Primary data.
Data file S2 (.m format). MATLAB code to identify the cycle.
Movie S1 (.mp4 format). Subject with transtibial amputation.
Movie S2 (.mp4 format). Subject with transfemoral amputation.

Materials and Methods

Finite element analysis (FEA)

The mechanical deformations and strain distributions in the Au sensor and entire device were obtained by FEA, using the commercial software ABAQUS (version 6.14, Standard). FEA involved two steps: (i) transformation from the 2D precursor to the 3D architecture without the encapsulation and (ii) addition of the encapsulation, thereby coupling deformations of the encapsulation to those of the 3D structure. Mesh refinement (> 7 million elements) ensured computational accuracy. To obtain the change in resistance of the Au strain gauge caused by deformation, a constant voltage was applied across the strain sensor. The resistance change of the gauge can then be calculated based on the current change. The elastic modulus and Poisson’s ratio used in the analysis were 119 GPa and 0.34 for Cu; 2.5 GPa and 0.34 for PI; 79 GPa and 0.42 for Au, 20 GPa and 0.34 for FR4, 70 kPa and 0.49 for the soft elastomer (Ecoflex 00-30, Smooth-on), and 5 MPa and 0.49 for the bottom adhesive layer (Argyle Hydrogel Adhesive Baby Tape Strips, Covidien).

Characterization of the pressure and temperature sensors

The setup for testing the pressure sensor (both wired and wireless) included a force gauge (M5-2, Mark-10) to measure the normal pressure, a digital multimeter (NI-USB 4065 Digital Multimeter) to measure the resistance of the sensor, and a motorized test stand (ESM303, Mark-10) to apply pressure with controlled loading and unloading rates (fig. S6). A dynamic mechanical tester (RSA-G2, TA Instruments) served as an alternative option for measuring the normal pressure and controlling the loading/unloading rates. Calibration of the temperature sensors used measurements with an infrared camera (FLIR A325SC, FLIR Systems) and a programmable hot plate to adjust the temperature. Tests of sensitivity to bending utilized a cylinder (6 cm in diameter) as a curved substrate for mounting the device. The setup for testing the shear stress also included a force gauge (M5-2, Mark-10) to measure the shear stress, a digital multimeter (NI-USB 4065 Digital Multimeter) to measure the resistance of the sensor, and a motorized test stand (ESM303, Mark-10) with two jaw-grip fixtures (G1013, Mark-10) to apply shear load. For simultaneous application of normal and shear loads, a force gauge oriented vertically measured and applied a normal pressure to the sensor, and another force gauge oriented horizontally and attached to a SiO_2 sputter-coated film of PI bonded to the top surface of the pressure sensor measured and applied a shear load to the sensor, simultaneously (fig. S11A).

Sampling frequency of the device

The response time of the sensor is about 0.16 s (Fig. 2I), corresponding to a bandwidth larger than 6 Hz. The maximum speed of the gaits observed in this study was 0.88 m/s, and the gait cycles were clear. For people without amputations, a walking speed of 0.9 m/s corresponds to a range of frequency from 1.3 to 1.7 Hz (*36*) while a step frequency of running is around 3.5 Hz for a speed of 5.6 m/s (*37*). Since prosthesis users often have slower speeds of movements than non-amputees (*38*), this wireless system can provide necessary information for most activities of people with amputations.

Temperature effect on the 3D pressure sensor

The temperature coefficient of resistance of the gold leads to a temperature sensitivity in the response of the pressure sensor. As demonstrated in fig. S21C, the 3D pressure sensor has the same temperature response with and without normal pressure. Therefore, the internal temperature sensor of the NFC SoC can serve as a reference to eliminate the temperature effect on the pressure performance using the following three equations obtained through separate measurements.

$$T = s \cdot ADC_t + c_1, \tag{1}$$

where T is temperature, ADC_t is the value from ADC channel of the NFC SoC that corresponds to temperature, and s and c_1 are calibration factors obtained from a water-bath experiment in which ADC_t values are recorded as a function of T.

$$ADC' = m \cdot T + c_2, \tag{2}$$

where ADC' is value from ADC channel for pressure when the pressure is zero, and m and c_2 are obtained from a water-bath experiment in which ADC' values are recorded as a function of T.

$$P = n \cdot (ADC - ADC') \tag{3}$$

where P is pressure, ADC is value from ADC channel of pressure and n is obtained from a pressure calibration experiments in which ADC values are recorded as a function of applied pressure measured with a force gauge performed at room temperature.

Combining Equations 2 and 3 gives Equation 4 by substituting ADC' from ADC. With this equation, an accurate measure of pressure can be determined at any temperature.

$$\begin{aligned} P &= n \cdot (ADC - ADC') \\ &= n \cdot (ADC - m \cdot (s \cdot ADC_t + c_1) - c_2) \end{aligned} \tag{4}$$

Incompatibility of the reference sensor

Several possibilities include (i) the fit of the prosthesis simulator, which could have influenced the pressure values, (ii) crimping of the cables of the reference sensor, which could have caused malfunctioning, (iii) anatomy of the lower limb, and (iv) differences in material properties between the reported sensor and the reference sensor. The GM muscle is a location where pressures are lower than those at bony prominences *(32)*. As a consequence, the pressure exhibited at the interface between the socket and skin at the GM is low (*22*). The lower limit of detection for the reference pressure sensor is 10 kPa. As a result, the reference sensor fails to capture pressure values on the GM (fig. S23E). Non-planar surfaces of the TT and FH can lead to small gaps between the soft, thin pressure sensors reported here and the planar reference devices due to the differences in their geometries and mechanical properties. These and related effects may lead to differences in the pressure readings from the FH during leg flexing and walking (fig. S23, F and G). Other testing configurations, such as placing different pressure sensors side by side, were not considered as every location on a residual lower limb has differences in the skin-socket interface. As a result, slight differences in location can lead to large differences in measurement results, as shown in fig. S23, H and I.

Voltage drop artifacts

The communication system involves two separate schedules: one on the NFC sensor for ADC sampling, and the other on the NFC reader for acquiring the data from the NFC sensor. The sensor cannot respond to the reading command when the NFC reader is polling data, as the system is busy sampling and storing the data into the non-volatile onboard memory. Potential countermeasures involve (i) reducing the sampling rate of the sensor, and (ii) reducing the reading out frequency of the NFC reader.

Supplementary figure S26 shows the outputs from the ADC at two sampling rates. At a sampling frequency of 10 Hz, voltage drops occur every ~20 s (fig. S26A). Decreasing the sampling frequency to 2.5 Hz completely eliminates these drops (fig. S26B). For monitoring quasi-static pressures, a sampling rate of 2.5 Hz is sufficient, and drops disappear. For highly dynamic changes in pressure, a sampling rate of 10 Hz is more appropriate, and the voltage drops can be removed by post-processing.

MATLAB codes for removing voltage drops

A customized MATLAB code locates the voltage drops and removes them by averaging the data from adjacent cycles to represent the signals during the voltage drops (fig. S27, A and B). For instance, the algorithm identifies the voltage drops through negative peak finding function (MATLAB; data file S2) with a threshold value of 50 kPa (i.e. the minimum amplitude difference between a peak and its neighbors is larger than 50 kPa, magenta dots in fig. S27, C to E). Calculation of the duration between positive local maxima defines the cycle. These local maxima (blue dots in fig. S27E) are defined through a positive peak finding function (MATLAB) with two parameters: (1) positive peaks with values larger than 200 kPa (MinPeakHeight of 200); (2) the largest peak among a group of peaks with time differences smaller than 0.3 s (MinPeakDistance of 0.3). For different subjects and different motions, the threshold values can be different.

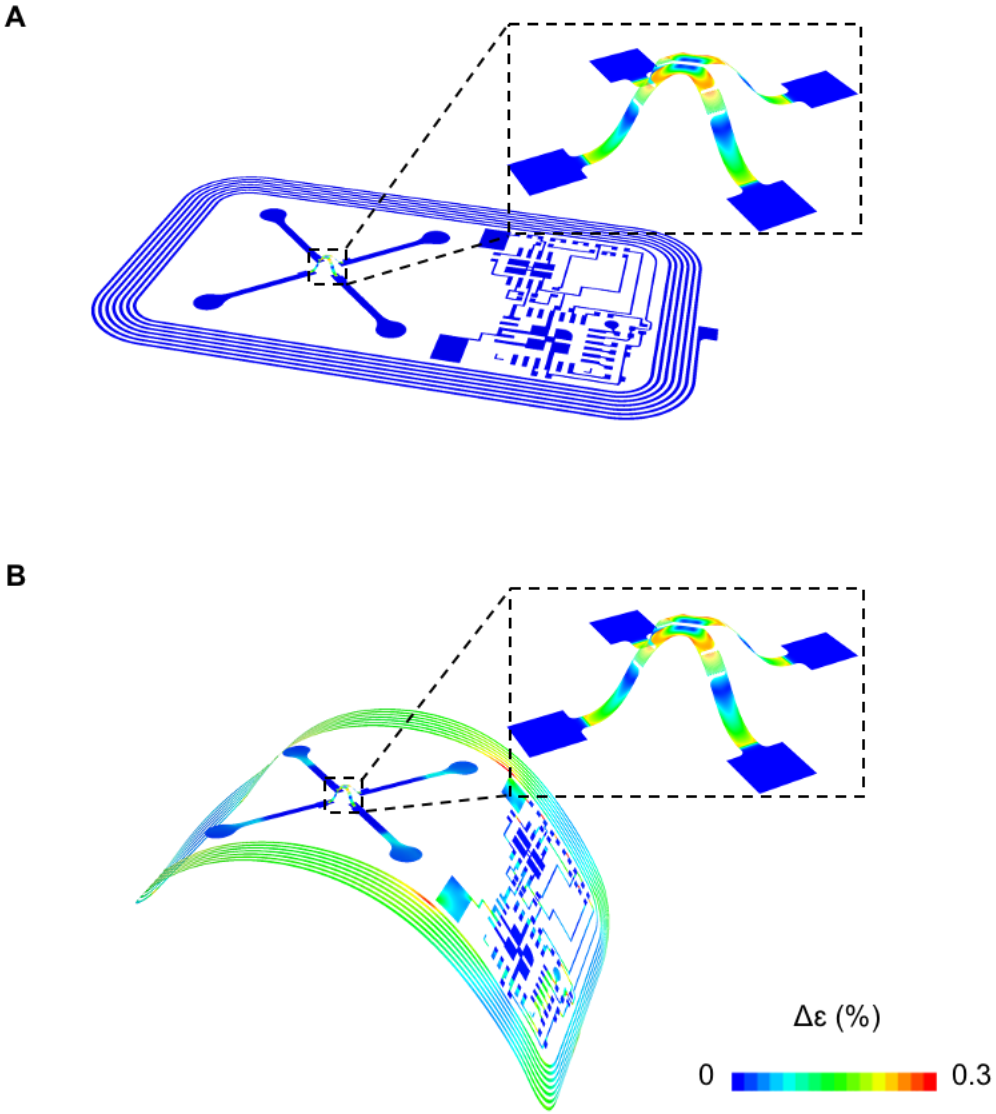

Fig. S1. Simulated distributions of strain in the Cu/Au layers. (**A**) The load-free state and (**B**) the bending state. Boxed regions show at higher magnification in insets.

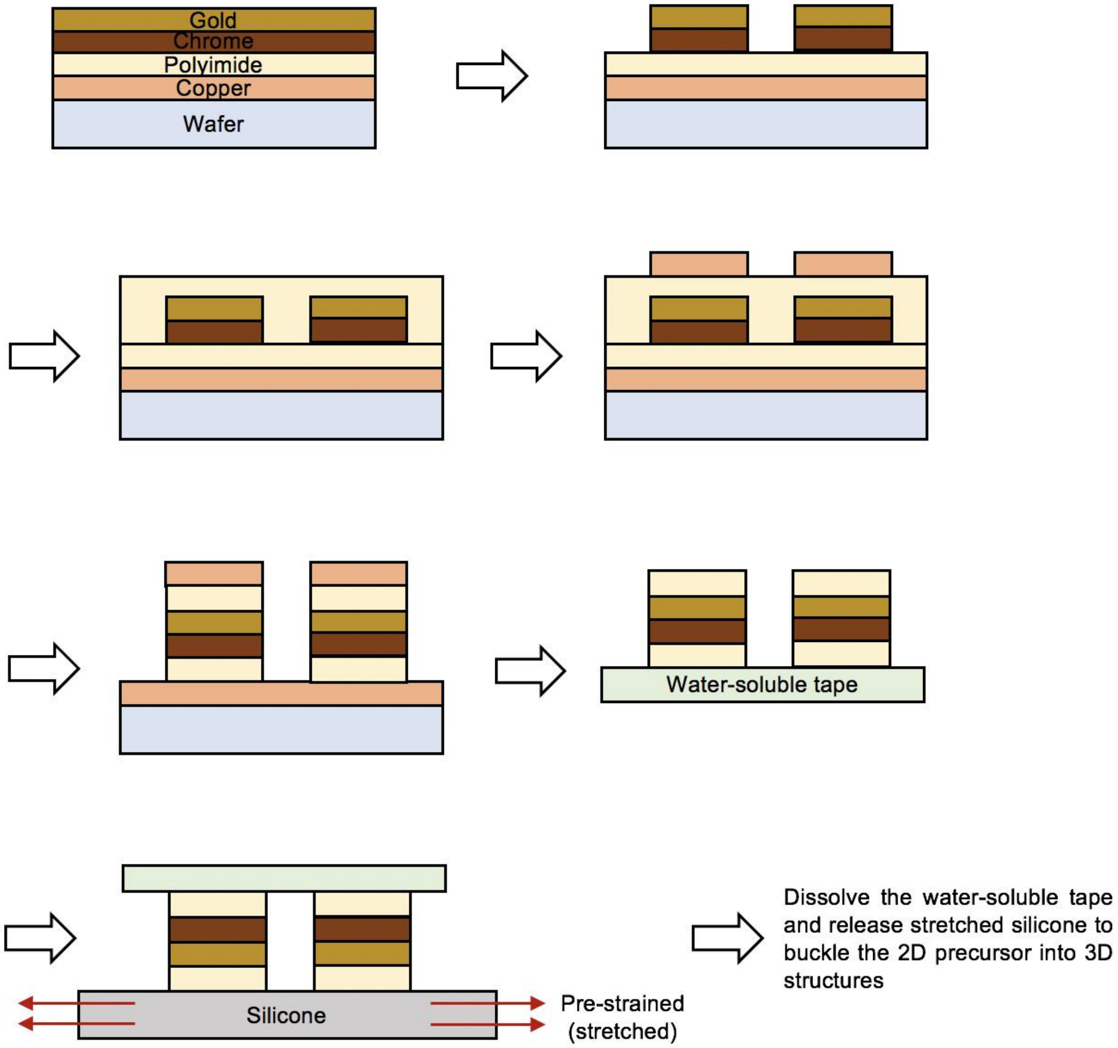

Dissolve the water-soluble tape and release stretched silicone to buckle the 2D precursor into 3D structures

Fig. S2. Schematic illustration of the process for fabricating the sensor.

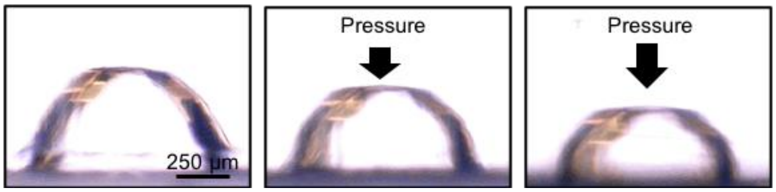

Fig. S3. Cross-sectional views. Pressure sensor under different normal pressure loads.

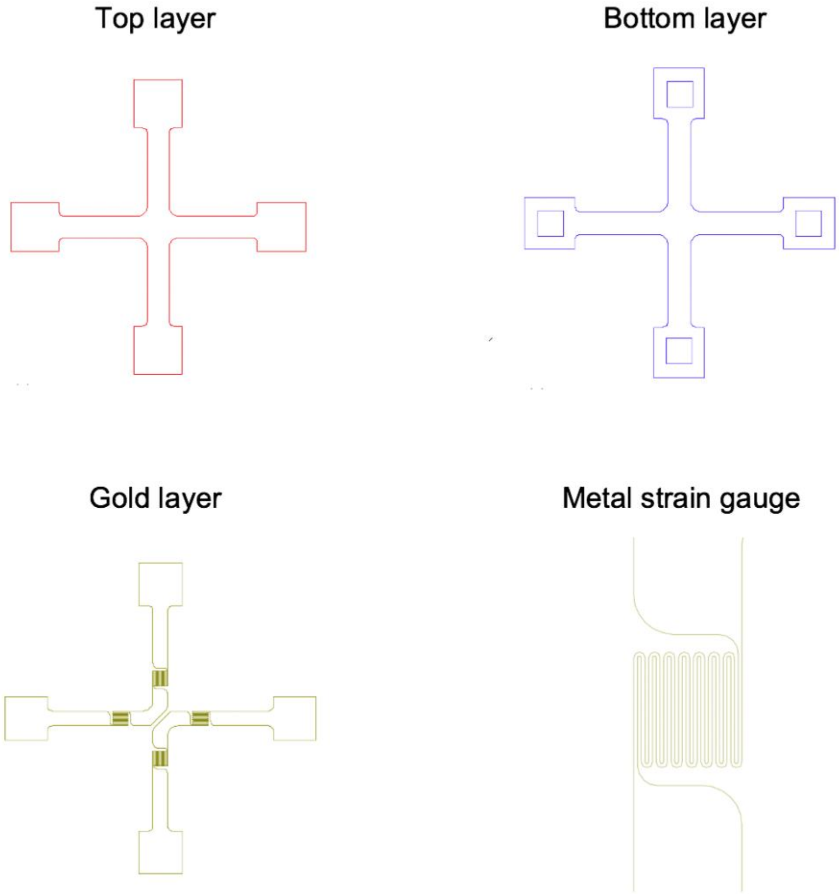

Fig. S4. 2D layout of the sensor.

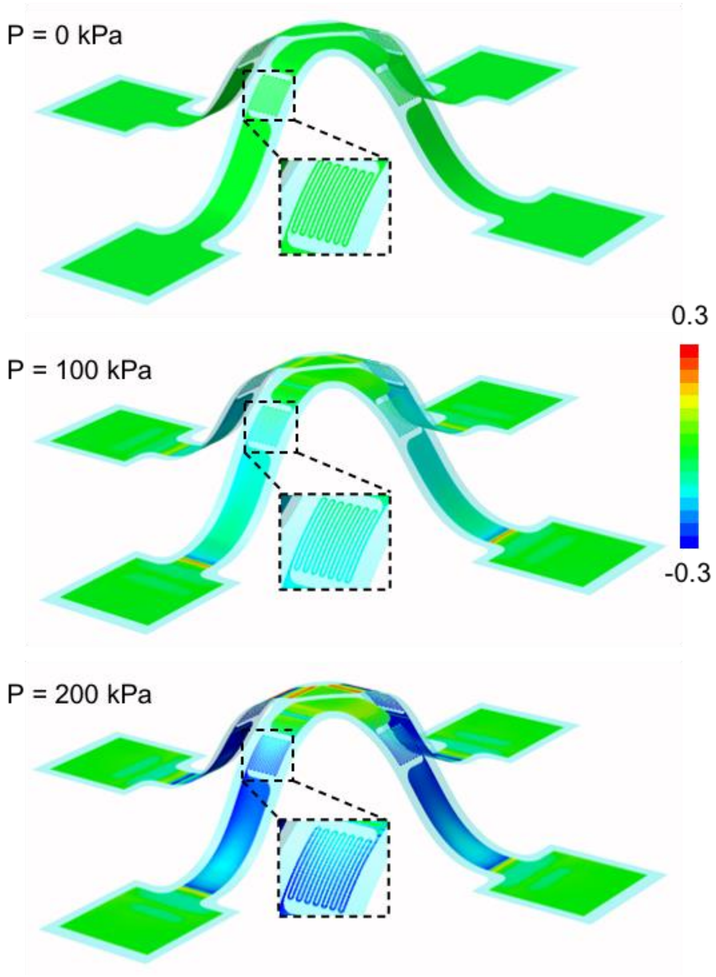

Fig. S5. Simulation of distributions of changes in strain. For the pressure sensor (*E*=2.6 MPa and 20% compression) under a normal pressure, *P*. Boxed regions are shown at higher magnification in insets.

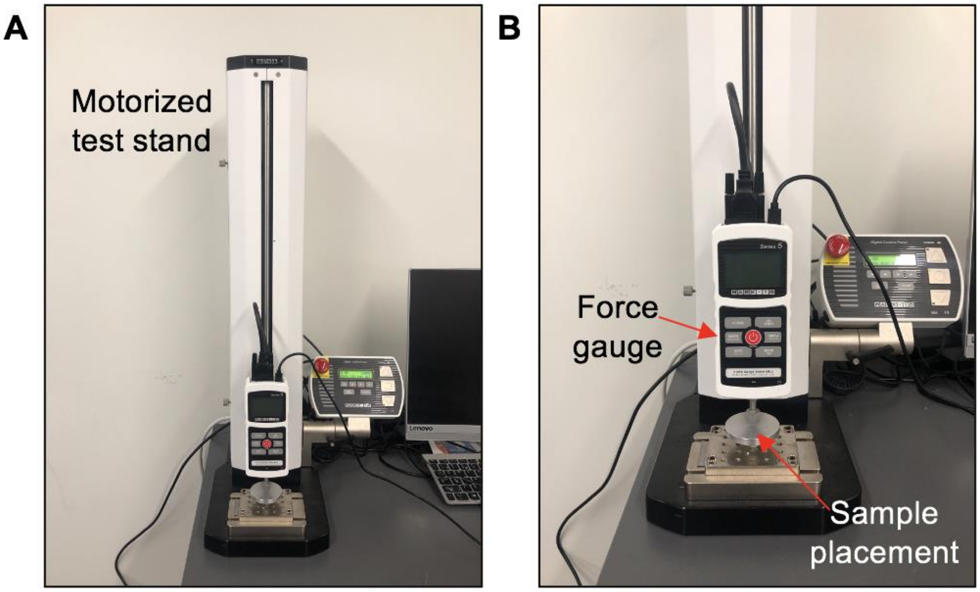

Fig. S6. Optical image of the measurement setup and equipment. (**A**) Image of the motorized test stand with the attached force gauge. (**B**) Image of the force gauge and the sample placement holder.

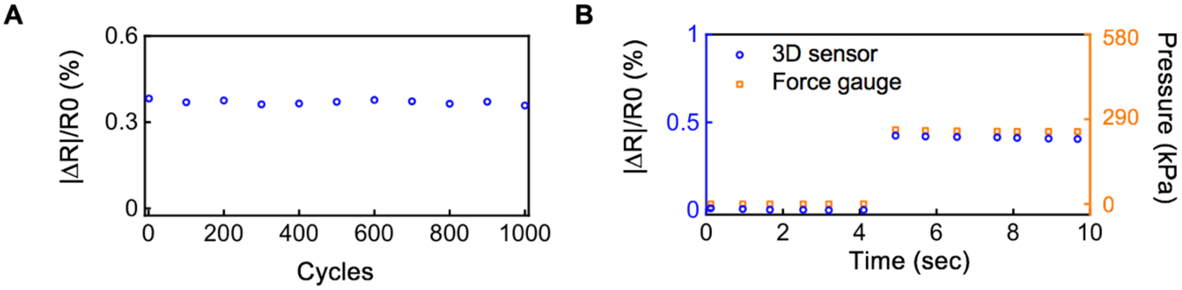

Fig. S7. Additional performance characteristics of the 3D pressure sensors. (**A**) Fractional change of resistance at different stages during measurements under cycles of loading and unloading (1000 cycles). (**B**) Fractional change of resistance during applied pressure. Sensor measurements compared to force gauge.

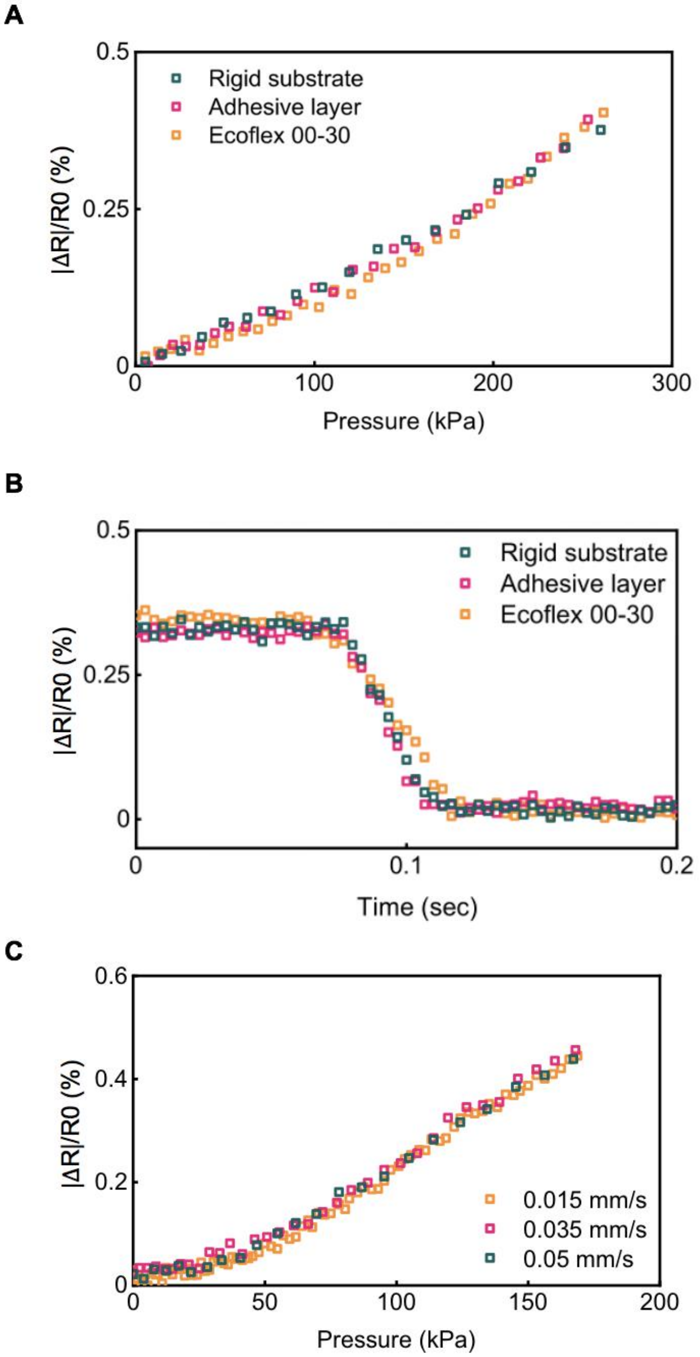

Fig. S8. Additional performance characteristics of the 3D pressure sensors under various settings. (**A**) Responses of a pressure sensor with different soft layers underneath. (**B**) Response times of a pressure sensor with different soft layers underneath. (**C**) Response of a pressure sensor under different loading rates.

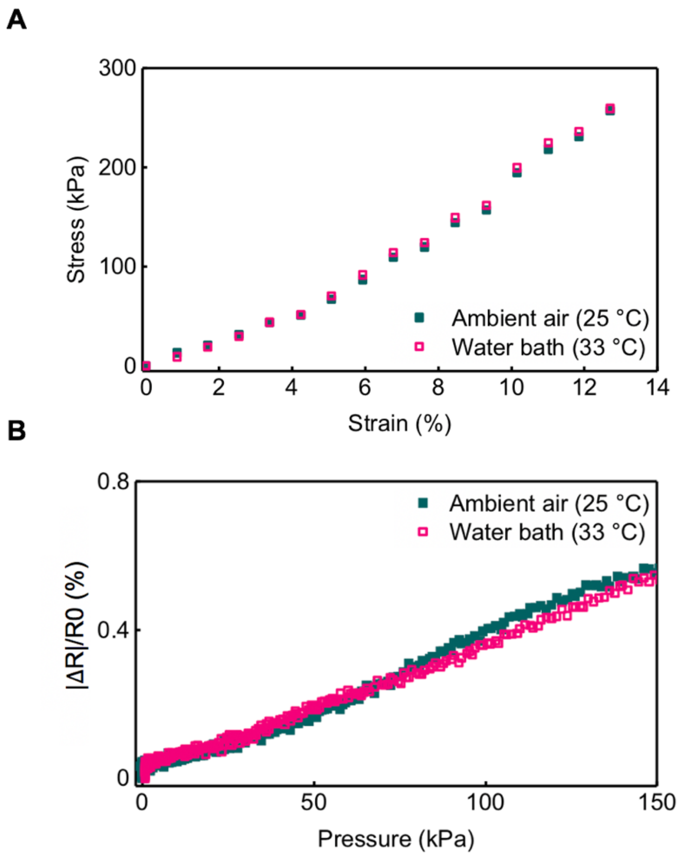

Fig. S9. Characteristics of the encapsulation layer and pressure sensor in two different thermal and humidity conditions. (**A**) Modulus of PDMS in ambient air (25 °C) and in a water bath (33 °C). (**B**) Responses of the pressure sensor in ambient air (25 °C) and in a water bath (33 °C).

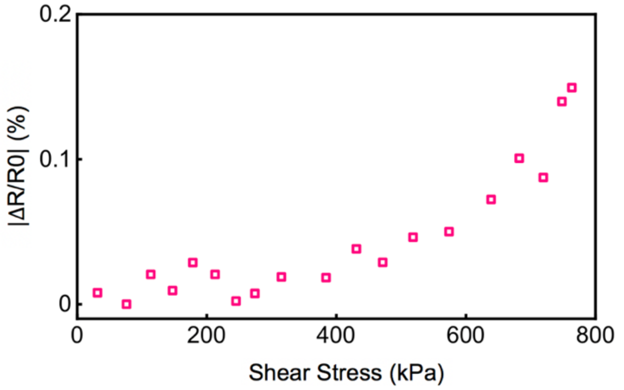

Fig. S10. Response of the sensor under shear stress.

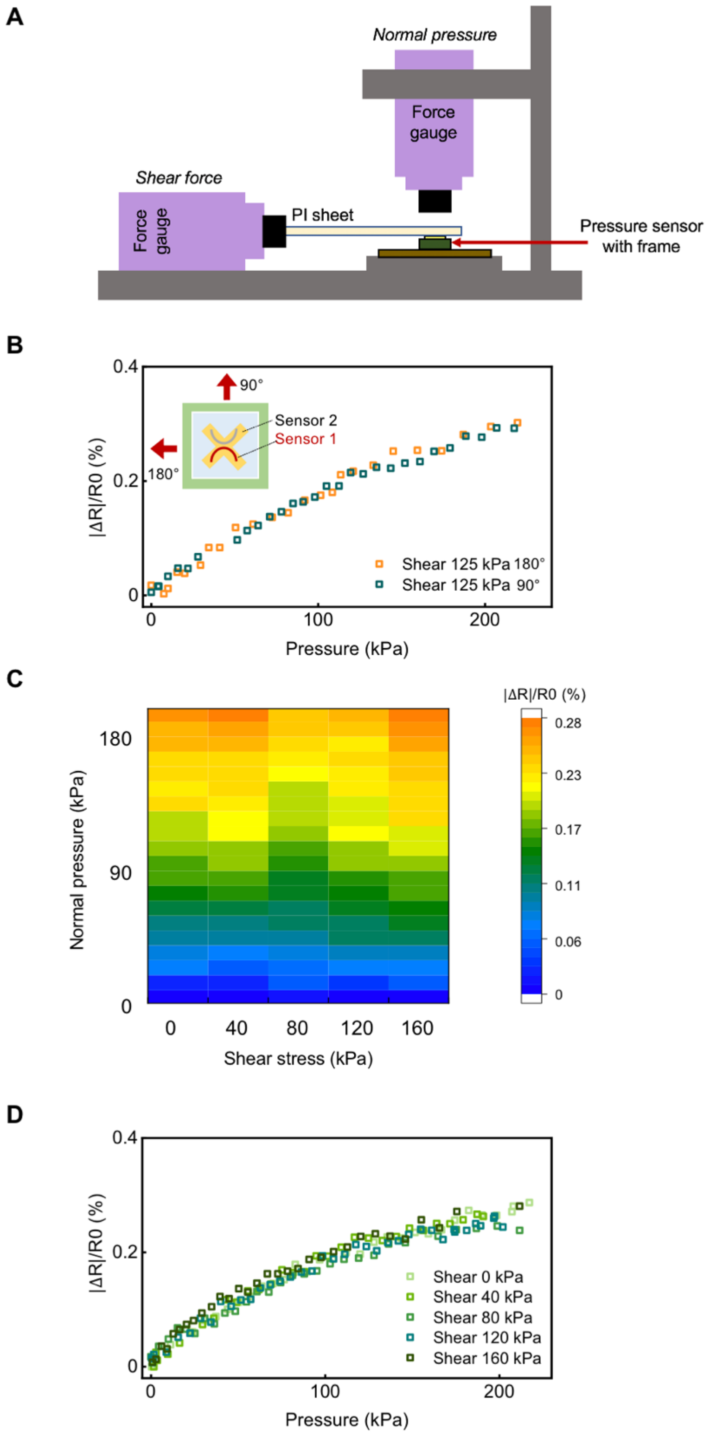

Fig. S11. Sensor performance to normal pressure under different shear stresses. (**A**) Testing setup for simultaneous application of normal and shear loads. (**B**) Response of sensor to normal pressure at the same shear load with different orientations (90 and 180 degrees) (**C**) Matrix chart of resistance change of the sensor to normal pressure at different shear loads (180 degrees). (**D**) Fractional change of resistance of the sensor to normal pressure at different shear loads (180 degrees).

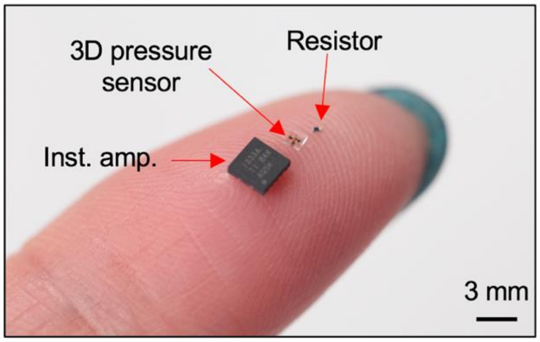

Fig. S12. Optical image of a pressure sensor. With commercial electronic components on fingertip.

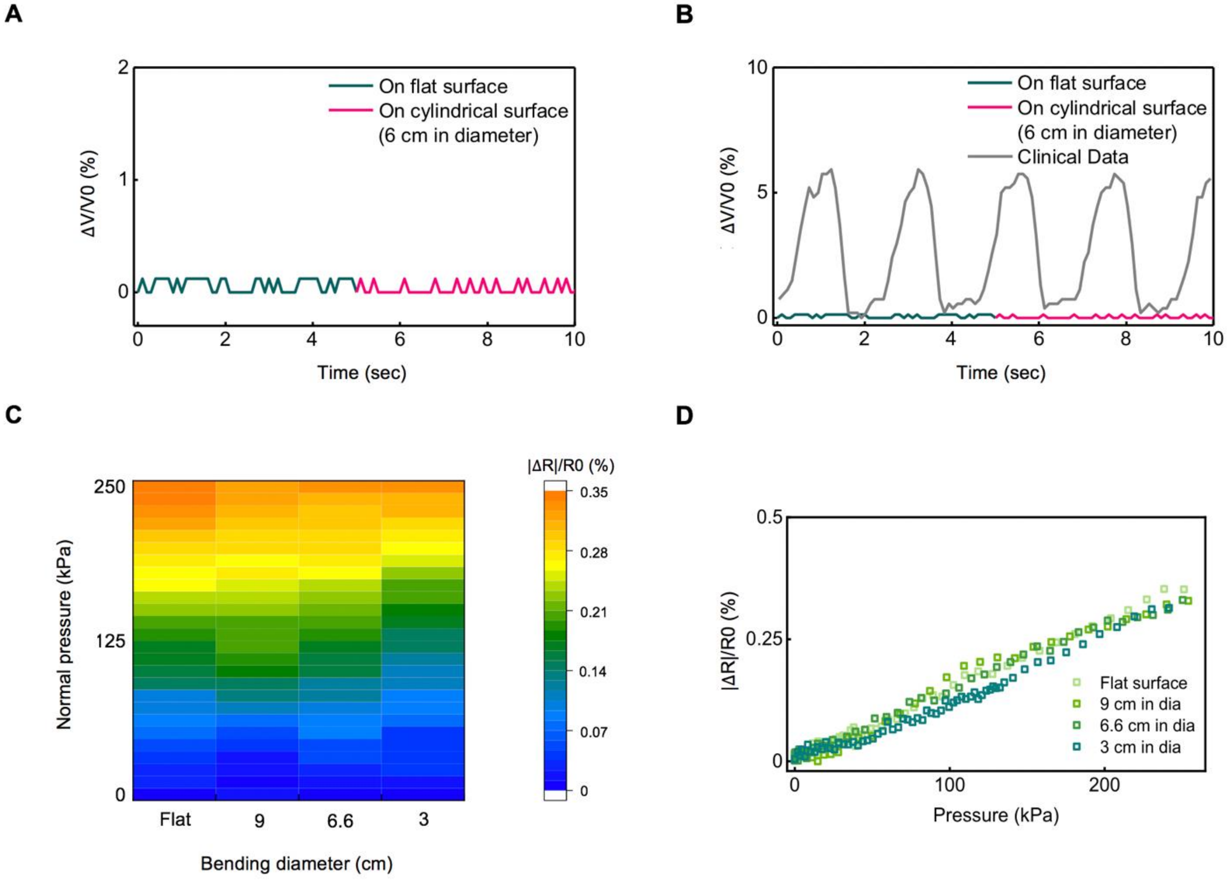

Fig. S13. Bending insensitivity of the sensor with the structural support. (**A**) Output of the device when placed on flat and curvilinear surfaces. (**B**) Output of the device during a clinical trial, indicating a large amplitude associated with changes in the ADC value. (**C**) Matrix chart of the resistance change of the sensor as a function of normal pressure at different bending diameters. (**D**) Fractional change of resistance of the sensor to normal pressure at different bending diameters.

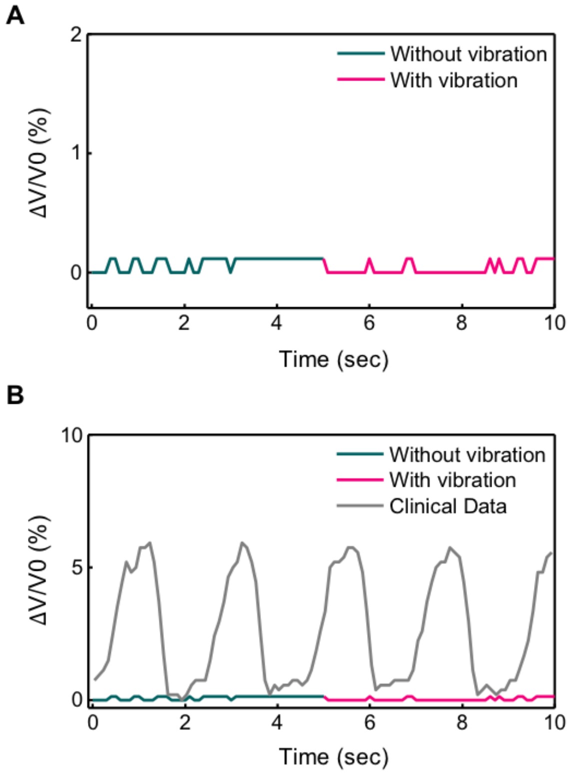

Fig. S14. Measurements that indicate an insensitivity to low-frequency vibrations. (**A**) Output of the device during vibration. (**B**) Output of the device during a clinical test, indicating a large amplitude associated with changes in the ADC value.

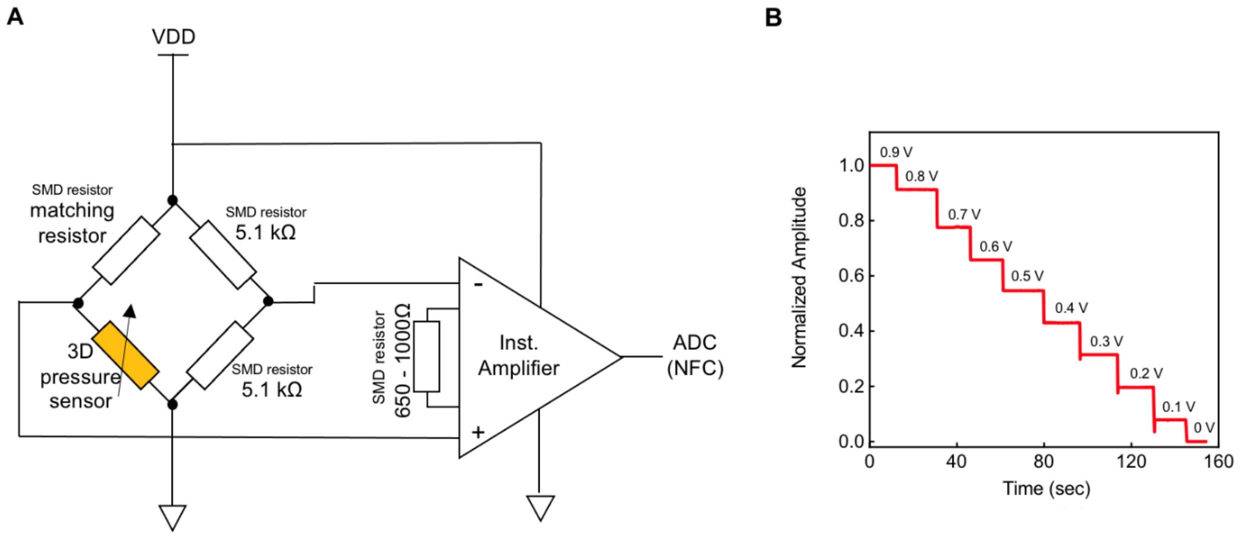

Fig. S15. Additional information about the circuit. (**A**) Circuit diagram of the device. (**B**) ADC output values based on voltage input.

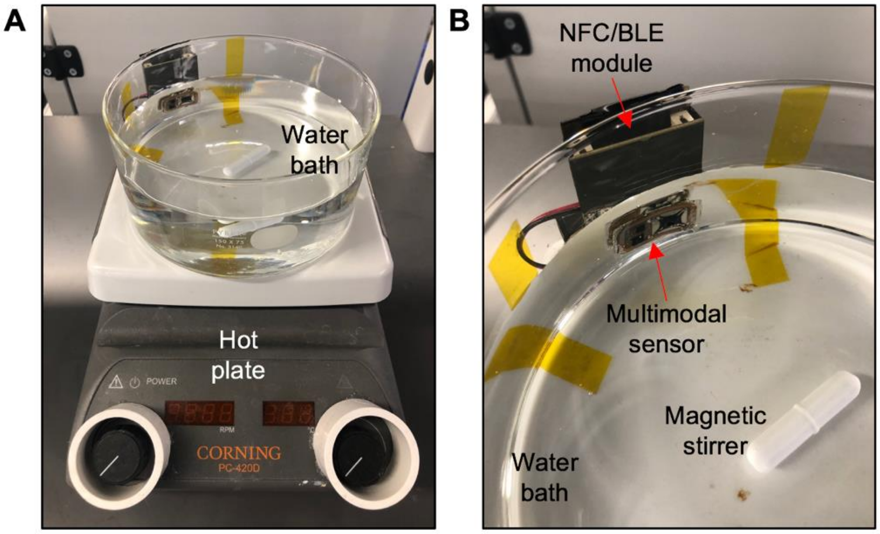

Fig. S16. Images of the multimodal device operated in water.

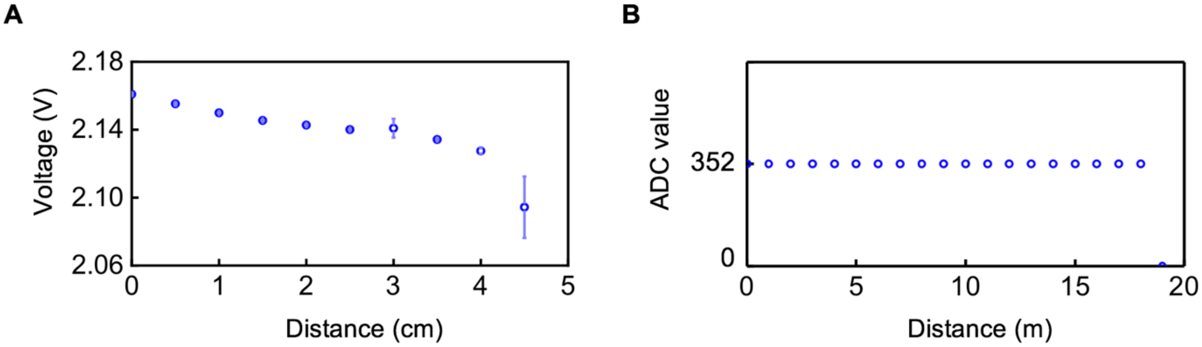

Fig. S17. Device specifications of communication distances. (**A**) Dependence of the ADC voltage on distance between two antennas. (**B**) Communication range between the device and the reader.

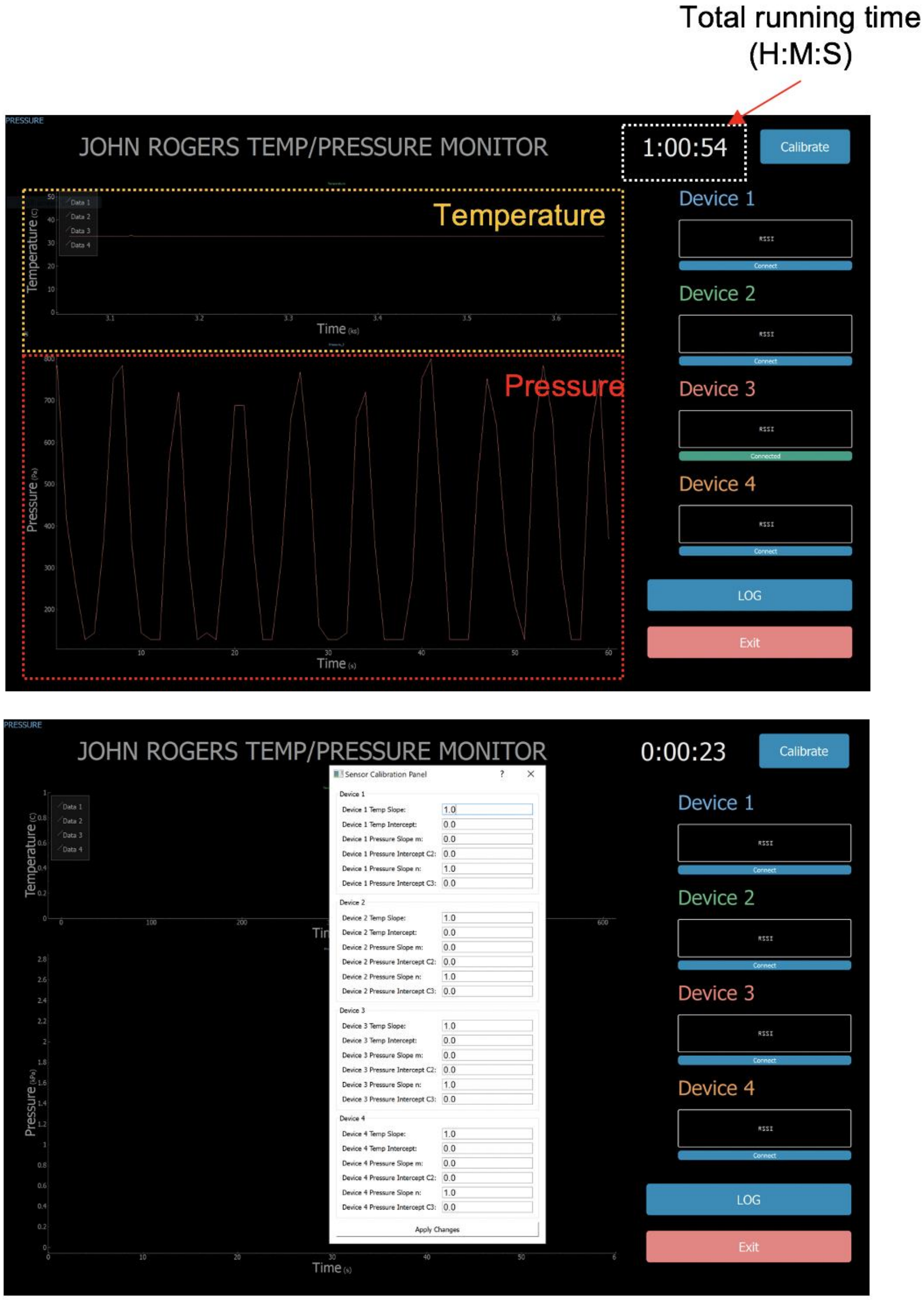

Total running time (H:M:S)

Device 1
Device 1 Temp Slope: 1.0
Device 1 Temp Intercept: 0.0
Device 1 Pressure Slope m: 0.0
Device 1 Pressure Intercept C2: 0.0
Device 1 Pressure Slope n: 1.0
Device 1 Pressure Intercept C3: 0.0

Device 2
Device 2 Temp Slope: 1.0
Device 2 Temp Intercept: 0.0
Device 2 Pressure Slope m: 0.0
Device 2 Pressure Intercept C2: 0.0
Device 2 Pressure Slope n: 1.0
Device 2 Pressure Intercept C3: 0.0

Device 3
Device 3 Temp Slope: 1.0
Device 3 Temp Intercept: 0.0
Device 3 Pressure Slope m: 0.0
Device 3 Pressure Intercept C2: 0.0
Device 3 Pressure Slope n: 1.0
Device 3 Pressure Intercept C3: 0.0

Device 4
Device 4 Temp Slope: 1.0
Device 4 Temp Intercept: 0.0
Device 4 Pressure Slope m: 0.0
Device 4 Pressure Intercept C2: 0.0
Device 4 Pressure Slope n: 1.0
Device 4 Pressure Intercept C3: 0.0

Fig. S18. Screenshot of the GUI.

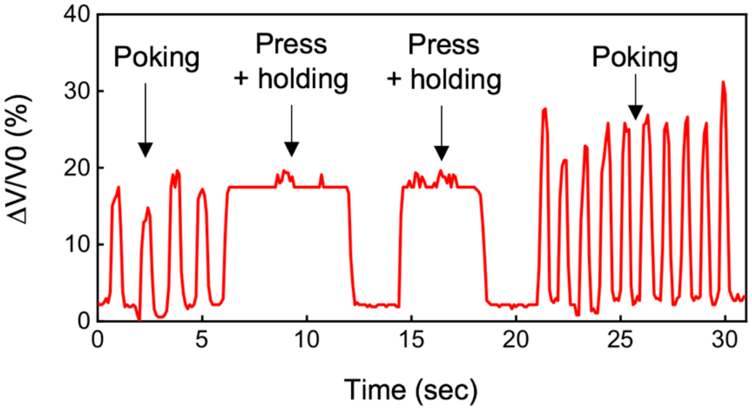

Fig. S19. Responses of the wireless device under different mechanical stimuli.

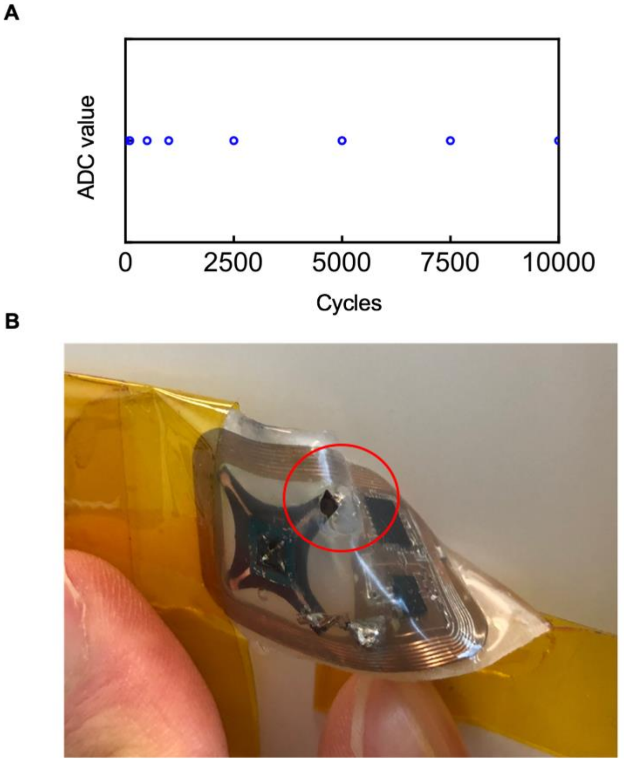

Fig. S20. Device under compressive bending. (**A**) Performance under multiple cycles of compressive bending. (**B**) Breakage of the device due to excessive compressive bending.

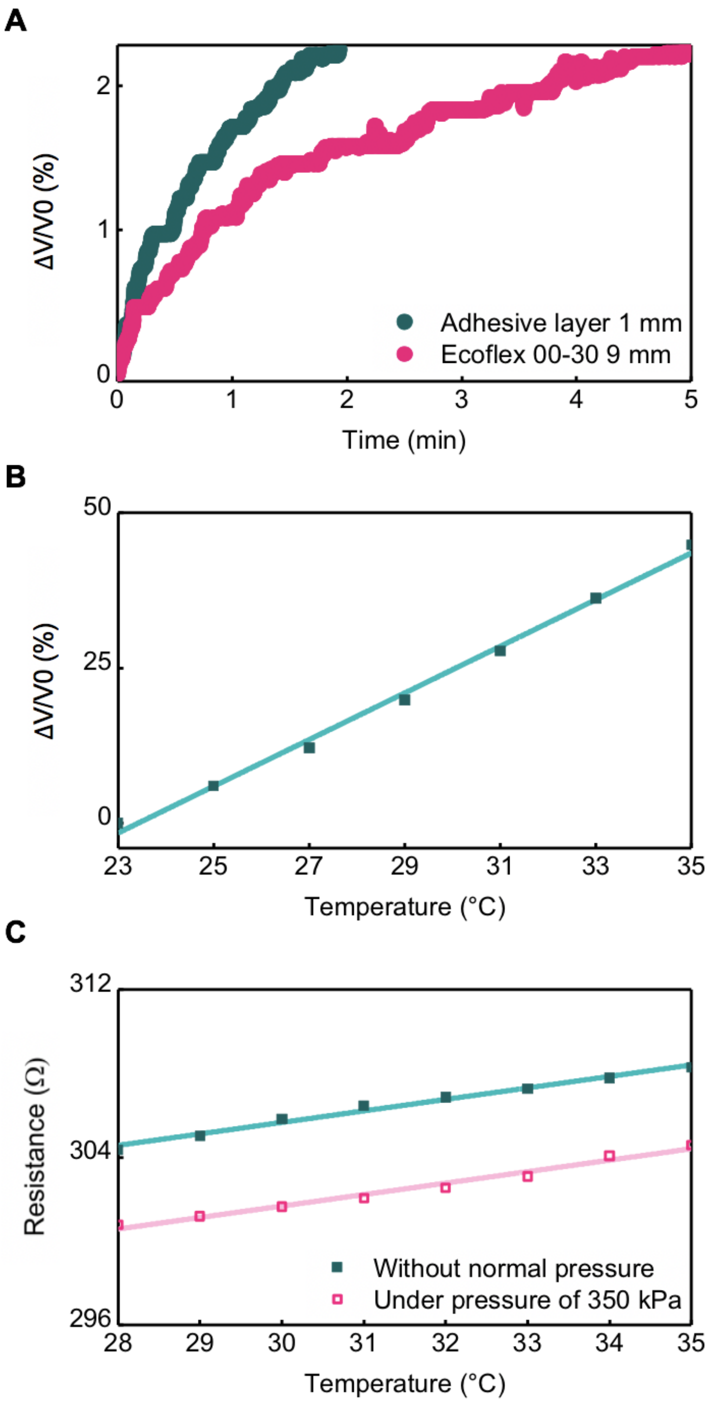

Fig. S21. Thermal characteristics of the on-chip temperature sensor and the 3D pressure sensor. (**A**) Frequency responses of the on-chip temperature sensor with different soft layers underneath. (**B**) Voltage change of a wireless pressure sensor in response to temperature when the applied pressure is zero. (**C**) Temperature response of the pressure sensor with and without normal pressure.

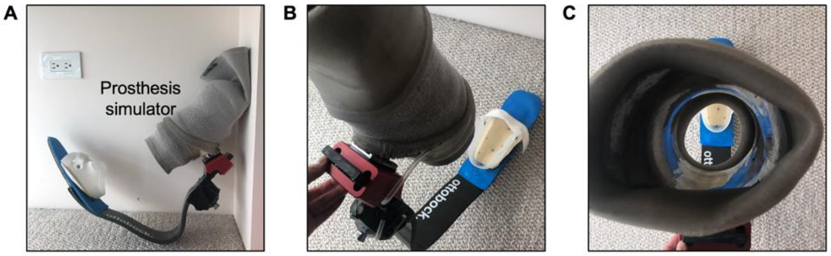

Fig. S22. Optical images of a prosthesis simulator. (**A**) Full image of the prosthesis simulator. (**B**) Detailed image showing where a foot is placed. (**C**) Top view showing where a lower limb is inserted.

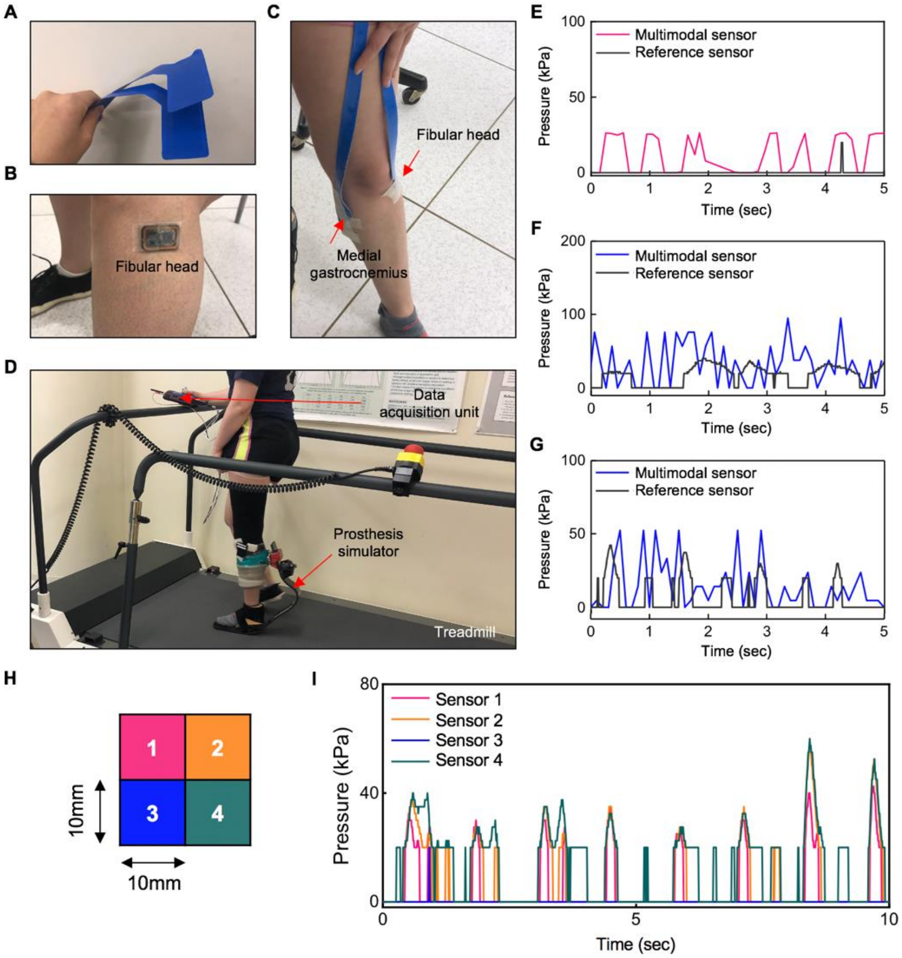

Fig. S23. Optical images and additional pressure data of comparison testing. (**A**) Sensing part of the two reference sensors. (**B**) Device mounted on a fibular head on a non-amputee subject. (**C**) Two locations, fibular head and medial gastrocnemius, where the reference sensors were placed on top of the devices. (**D**) A non-amputee subject walking on a treadmill, wearing a prosthesis simulator over two reference sensors and two devices while holding a data acquisition unit for the reference sensors for the comparison testing. (**E**) Pressure comparison data to a reference during walking (gastrocnemius), (**F**) flexing (fibular head), and (**G**) walking (fibular head). (**H**) Sectional schematic illustration of the reference sensor. (**I**) Data on the sensor mounted on the fibular head of a subject without amputation during walking.

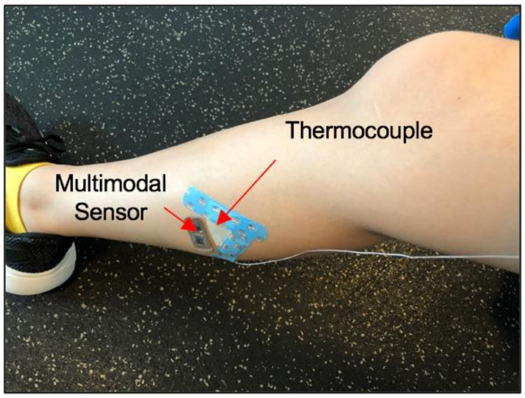

Fig. S24. Optical images of the temperature comparison test.

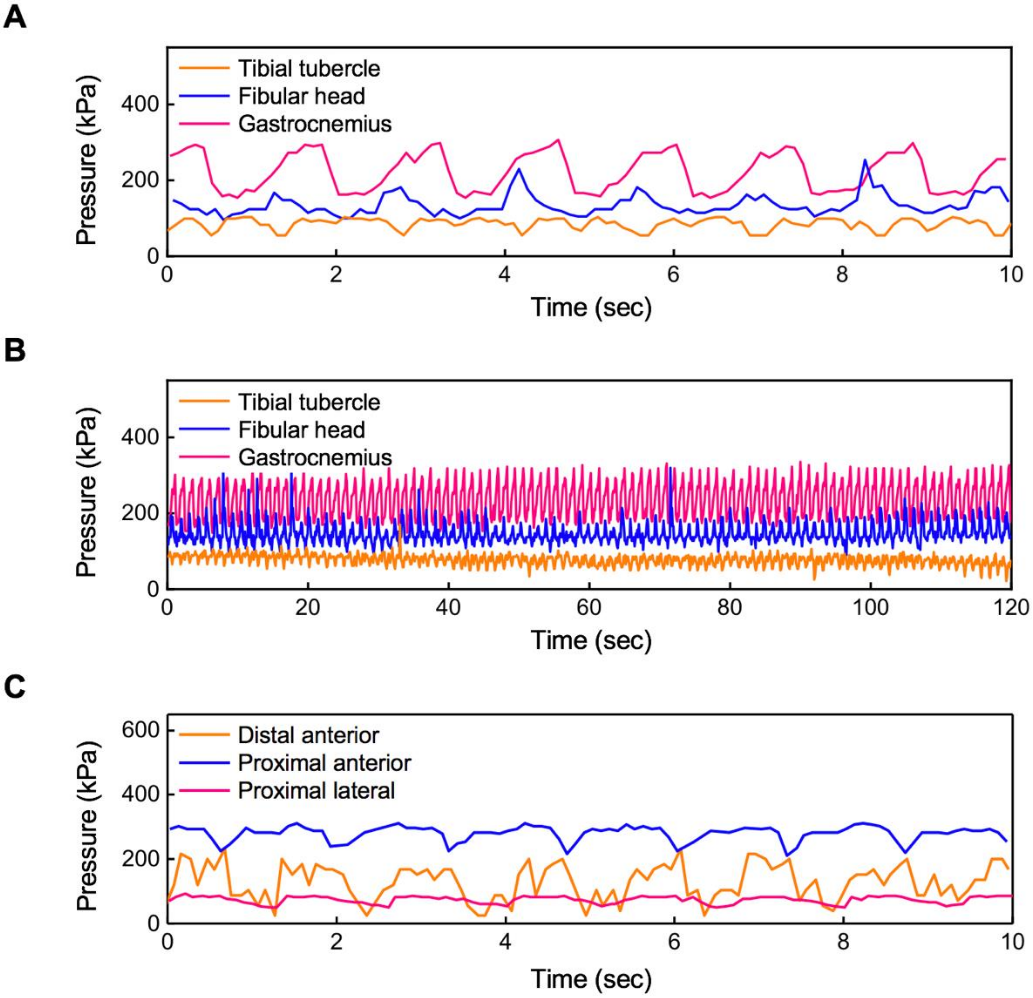

Fig. S25. Additional pressure data from subjects. Data from a subject with transtibial amputation of (**A**) 10 s and (**B**) 120 s. (**C**) Data from a subject with transfemoral amputation of 10 s.

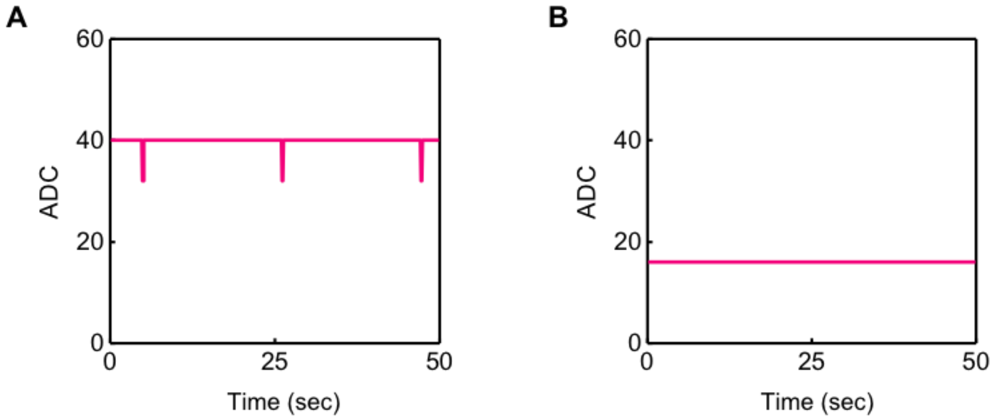

Fig. S26. Wirelessly powered ADC output at different sampling rates. (**A**) 10 Hz. (**B**) 2.5 Hz.

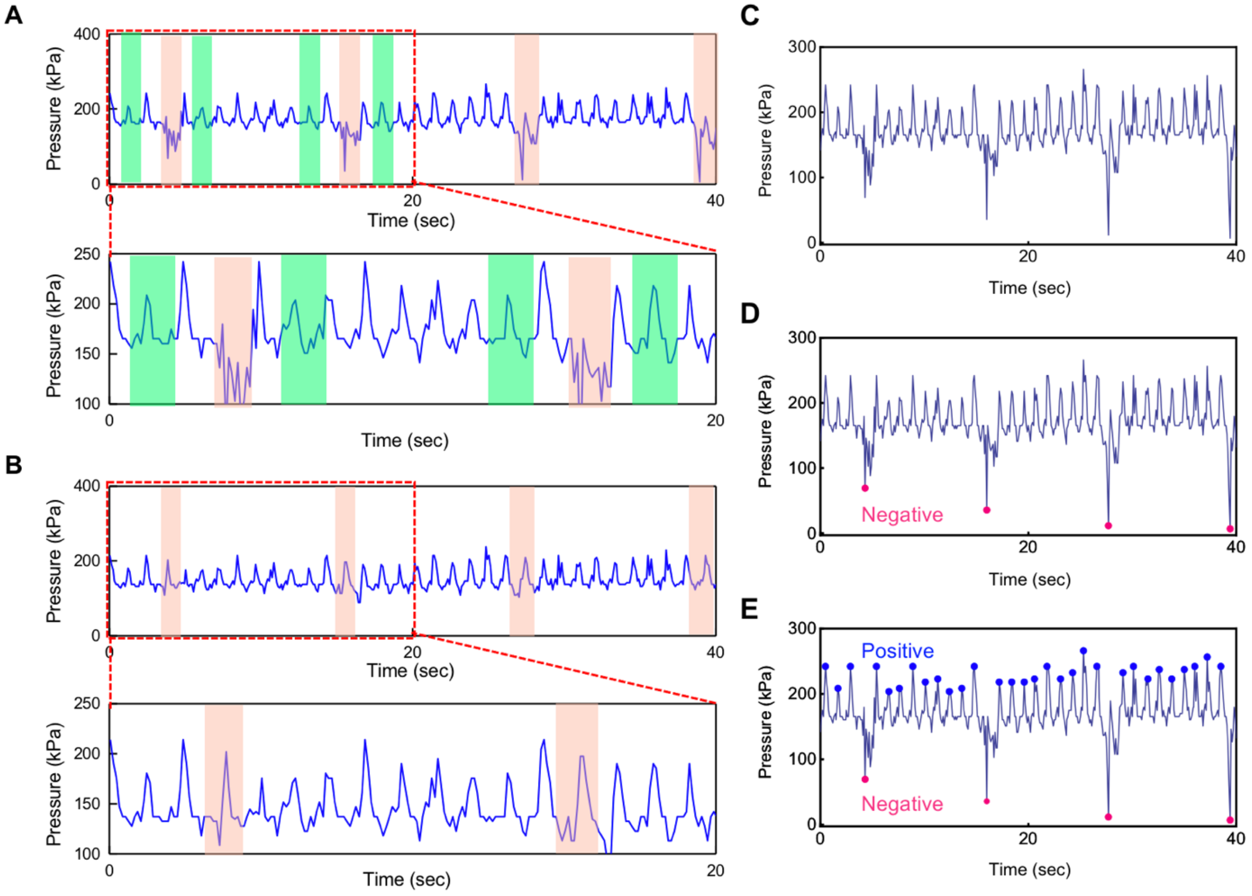

Fig. S27. Postprocessing of data using MATLAB. (**A**) Original data, where green regions indicate the selected adjacent cycles and coral regions indicate the voltage drops. (**B**) Data after averaging. Drops are now removed as coral regions show. (**C-E**) Steps to define cycles using algorithms available in MATLAB. With (**C**) raw data, (**D**) find drops, where negative peaks (magenta dots) indicate drops. Then, (**E**) define cycles with positive peaks (blue dots).

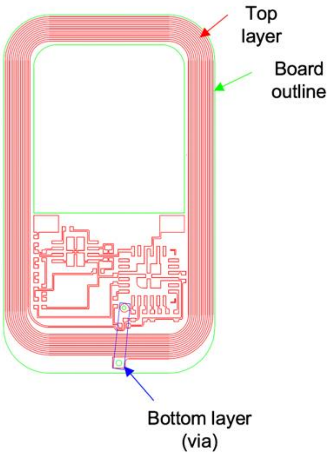

Fig. S28. CAD design of the NFC circuit.

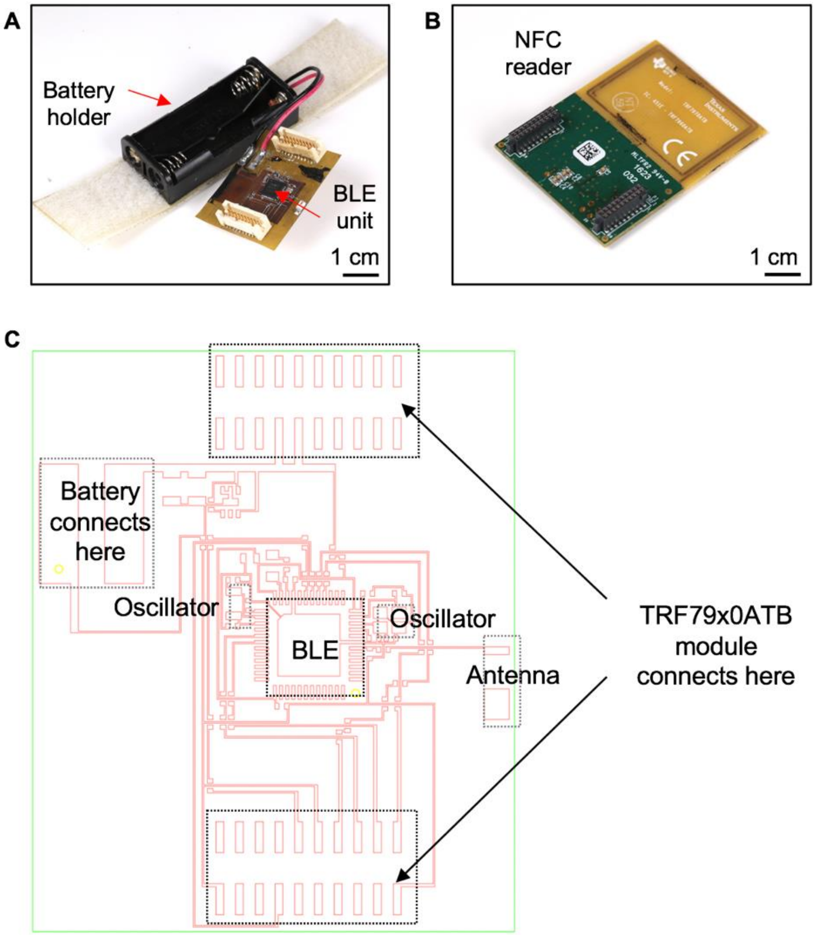

Fig. S29. Hybrid NFC/BLE module. (**A**) Optical image of the BLE unit attached to a battery holder. (**B**) Optical image of the NFC reader. (**C**) CAD design of the BLE unit of the module.

Table S1. Summary of participants for clinical trials.

	Amputation	Age	Sex	Skin Irritation
1	None	25	F	N
2	None	27	F	N
3	Transtibial	43	F	N
4	Transfemoral	49	F	N

Supplementary videos

Movie S1. Subject with transtibial amputation. Recording from a subject with transtibial amputation who is walking on a treadmill, where pressure on each anatomic location is captured by three sensing devices placed on a lower limb inside a prosthesis, as displayed on a tablet.

Movie S2. Subject with transfemoral amputation. Recording from a subject with transfemoral amputation who is walking on a treadmill, where pressure on each anatomic location is captured by three sensing devices placed on a lower limb inside a prosthesis, as displayed on a tablet.